Control over Position, Orientation, and Spacing of Arrays of Gold Nanorods Using Chemically Nanopatterned Surfaces and Tailored Particle–Particle–Surface Interactions
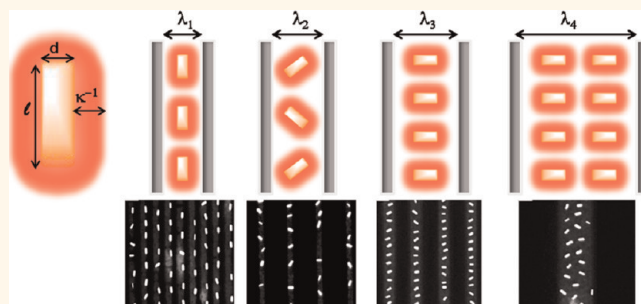
Dhriti Nepal,[†] M. Serdar Onses,[§] Kyoungweon Park,[†] Michael Jespersen,[†] Christopher J. Thode,[§] Paul F. Nealey,[§] and Richard A. Vaia[†,*]

[†]Nanostructured and Biological Materials Branch, Air Force Research Laboratories/RXBN, Wright-Patterson AFB, Ohio, United States and [§]Department of Chemical and Biological Engineering, College of Engineering, University of Wisconsin—Madison, Madison, Wisconsin, United States

The uniform and hierarchical arrangement of nanoscopic structures across macroscopic length scales is a prerequisite for developing next-generation devices.[1,2] For example, the rich optical, electrical, and magnetic properties of periodic arrays of plasmonic nanoparticles promise ultrasmall platforms for antennas, filters, memory, energy generation devices, and logic circuits. These unique properties arise from coupling of localized surface plasmons and thus depend strongly on the interparticle distance (≪100 nm).[3,4] To achieve the requisite structural precision, most studies use top-down lithographic and deposition techniques including electron beam, scanning probes, and evaporation. However throughput, cost, poor surface roughness, and polycrystallinity of the resulting sub-100 nm structures limit direct exploitation in commercial fabrication processes. Alternatively, colloidal approaches based on directed and self-assembly concepts[5–12] provide intriguing alternatives to fabricate these translationally ordered nanoparticle arrays. Due to the solution chemistry approach, they offer numerous advantages such as compositionally asymmetric structures, atomically smooth surfaces, single-crystalline units, three-dimensional nanoscale gaps, and continuous fabrication. However these approaches lack the robustness to deliver complex spatial design inherent to traditional lithographic approaches, such as uniform interparticle spacing and rotational alignment along arbitrarily shaped lines with ultralow defect densities. The crucial challenge therefore is

how to best synergize the salient features of additive (directed and self-assembly) and subtractive (lithography) concepts to provide fabrication routes that cost-effectively enable these new device architectures in a green and environmentally benign way.

To address this challenge, recent efforts utilize lithographic techniques to define topographical templates or chemical contrast

ABSTRACT

The synergy of self- and directed-assembly processes and lithography provides intriguing avenues to fabricate translationally ordered nanoparticle arrangements, but currently lacks the robustness necessary to deliver complex spatial organization. Here, we demonstrate that interparticle spacing and local orientation of gold nanorods (AuNR) can be tuned by controlling the Debye length of AuNR in solution and the dimensions of a chemical contrast pattern. Electrostatic and hydrophobic selectivity for AuNR to absorb to patterned regions of poly(2-vinylpyridine) (P2VP) and polystyrene brushes and mats was demonstrated for AuNR functionalized with mercaptopropane sulfonate (MS) and poly(ethylene glycol), respectively. For P2VP patterns of stripes with widths comparable to the length of the AuNR, single- and double-column arrangements of AuNR oriented parallel and perpendicular to the P2VP line were obtained for MS-AuNR. Furthermore, the spacing of the assembled AuNR was uniform along the stripe and related to the ionic strength of the AuNR dispersion. The different AuNR arrangements are consistent with predictions based on maximization of packing of AuNR within the confined strip.

* Address correspondence to richard.vaia@wpafb.af.mil.
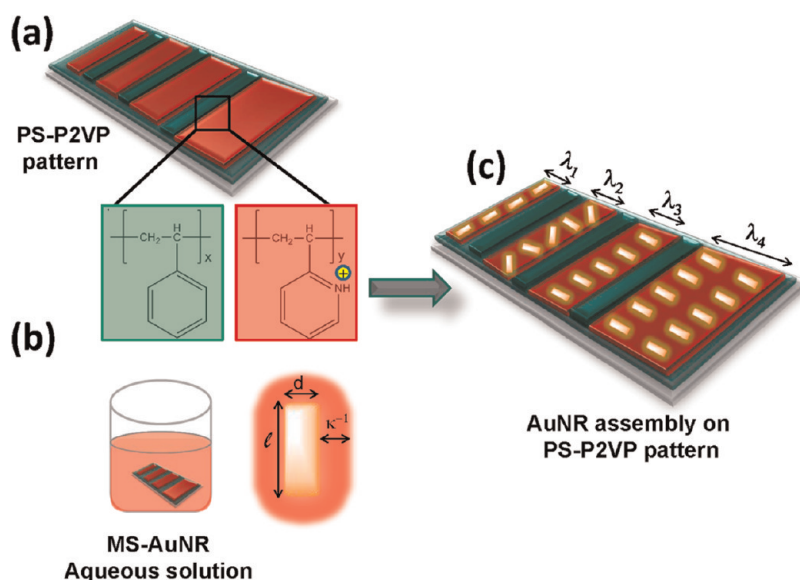
Figure 1. Schematic of the assembly of gold nanorods (AuNR) on chemically nanopatterned surfaces. Surface selectivity is based on electrostatic interaction. (a) Polymer-derived surface pattern of polystyrene (PS) and poly(2-vinylpyridine) (P2VP) is combined with (b) aqueous solution of mercaptopropane sulfonate-functionalized AuNR (MS-AuNR) to yield (c) preferential absorption and directed assembly of MS-AuNR on the P2VP features. The local orientation and spacing of the AuNR is controlled by confinement (P2VP feature width, λ) and Debye length (κ^{-1}) of the MS-AuNR (ℓ = length, d = diameter).

patterns, which are subsequently used to direct the assembly of nanoparticles.[13,14] In topographic assembly, pattern replication *via* the colloids is due to confinement of the deposition solution between troughs and ridges on the substrate due to surface tension. Close packing of the particles occurs due to the interparticle capillary forces, but extensive tunablility of nanoparticle spacing, multicomponent deposition, and minimization of processing defects is challenging.[15,16] Conversely, for a chemical contrast pattern, selectivity between nanoparticles and surface regions is established through complementary surface interactions such as hydrogen bonds,[17,18] biomacromolecular hybridization,[19] electrostatic forces,[20–22] or hydrophobic interactions.[23] These surface interactions afford substantial additional flexibility to direct the assembly process *via* tuning the interparticle interactions[22,24] by changing pH, ionic strength, or solvents.

Together, these directed assembly approaches have demonstrated control of position and interparticle spacing of a wide array of spherical particles across complex large-scale surface patterns.[13,14,20–22] To progress to smaller domains however, where the template is of a length scale commensurate with the particles, the impact of a confining potential on the assembly process and intrapattern order must be understood and utilized. Symmetry breaking and even induction of chirality have been demonstrated for packing of spherical colloids[25] and deposition of thin block copolymer films. However, there still is a lack of understanding of how confinement synergistically impacts both translational and orientational order of anisotropic units, such as rod-shaped nanoparticles. Prior topographic

template approaches have shown large arrays of close-packed nanoparticles[16] where the number of particles in each domain is controlled by decreasing the confinement.[15,26,27] In contrast, the impact of surface interactions and size of chemical contrast patterns for anisotropic particle assembly has not been explored.

Herein we demonstrate that the interplay of Debye length and the dimensions of chemical nanopatterns provides simultaneous control of both interparticle spacing and local orientation during surface assembly of anisotropic colloids (rods) from aqueous solutions. Specifically, parallel and perpendicular orientations of sodium sulfonate-functionalized gold nanorods (AuNR) were created on poly-2-vinylpyridine (P2VP) lines with a polystyrene (PS) background. The resultant patterns adopt integral arrangements of one, two, or three rods per feature width, in agreement with predictions assuming maximization of AuNR–P2VP interaction area.

RESULTS AND DISCUSSION

Figure 1 illustrates the process for investigating the assembly of nanoparticles on chemically nanopatterned surfaces. The steps consist of the creation of chemical patterns with sub-100 nm features, the synthesis of an aqueous dispersion of functionalized nanorods with high specificity to one surface, the incubation of the patterned substrate with the nanoparticle solution, and removal of nonspecifically bound nanoparticles by washing. To achieve the pattern dimensions comparable with the nanorods (10–100 nm), polymer-derived surface patterns (PDSPs) consisting of PS mats and P2VP brushes were fabricated as previously

reported.[28] In brief, a cross-linked PS mat was deposited on a silicon wafer, a resist was patterned on top of the mat using electron beam lithography, the PS mat was then selectively removed by etching, and finally the etched regions were backfilled by grafting end functional P2VP brushes. In parallel, aqueous dispersions of functionalized AuNR, including mercaptopropane sulfonate sodium salt (MS) and thiolated poly(ethylene glycol) (PEG), were synthesized following modifications of previously reported procedures.[29] Of note, place exchange reaction on AuNR with thiolated PEG is carried out first, since direct charge inversion from hexadecyltrimethylammonium bromide (CTAB)-stabilized AuNR (zeta potential $+42 \pm 1.0$ mV) to MS-stabilized AuNR (zeta potential -23.1 ± 0.5 mV) is not effective due to electrostatic interaction between MS and CTAB, leading to aggregation of AuNR. Finally, after submersion of the patterned substrates in the aqueous AuNR solution, the substrates are washed by sonication to remove weakly bound particles.

Creating high specificity of AuNR affinity toward one region of the chemical pattern and controlling the strength of that interaction are the most crucial elements for successful assembly of nanoparticle arrays. If the surface−particle interactions are too strong,[13,30] such as via room-temperature DNA hybridization, covalent bonding, or acid−base reactions, specificity is achieved at the expense of responsiveness of local particle order to the confining potential or mobility of previously absorbed particles to accommodate subsequent particle absorption. In these cases, the surface−particle binding is effectively irreversible, resulting in a random arrangement that is described by the random sequential adsorption model of sticky particles onto a sticky surface.[31,32] Structural refinement requires a postassembly anneal at conditions where the substrate particle interactions are sufficiently weakened. In contrast, if the particle−surface binding is too weak, subsequent processing to remove nonspecific binding may also remove a fraction of particles from the assembled regions, increasing defect density. Thus one-step fabrication of hierarchical structures with simultaneous local spatial and orientational order between particles and complex macroscopic features including lines, corners, and areas necessitates an intermediate degree of particle−surface attraction whose magnitude is comparable to the particle−particle repulsion maintaining solution stability of the nanoparticles. In the context of meeting these assembly constraints, Figure 2 and Table 1 summarize the specificity of PEG-AuNR and MS-AuNR to PS and P2VP regions with lateral dimensions greater than 100 times the nanorod length (50 nm).

PEG-AuNR (zeta $\approx -2 \pm 0.5$ mV) are sterically stabilized in aqueous solution and interact sufficiently strong with the PS surface such that a monolayer of particles remains absorbed after washing (Figure 2b).
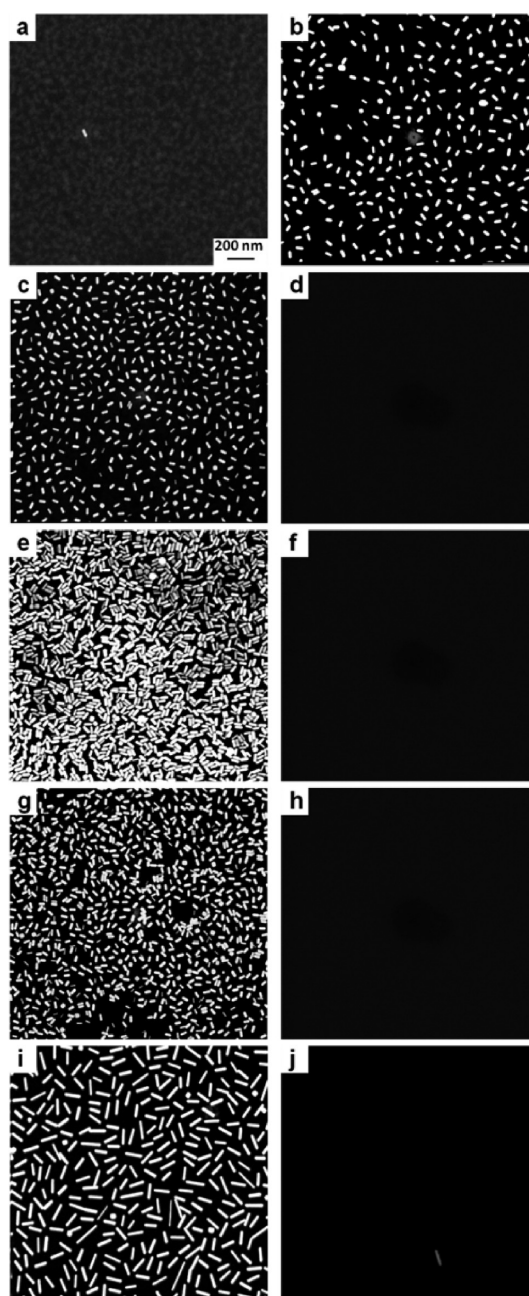
Figure 2. Selectivity of functionalized AuNR on different polymer substrates: P2VP (a, c, e, g, i) and PS (b, d, f, h, j). SEM images (scale bar = 200 nm) show PEG-AuNR has selective adsorption on PS (b) but not on P2VP (a), whereas MS-AuNR has the reverse selectivity (c, e, g, i). For a given AuNR aspect ratio (2.5; length = 47.8 ± 5 nm, diameter = 20.0 ± 3 nm), these images show the impact of electrolyte content, (c) MS-AuNR (I_{low} = 0.2 mM NaCl) and (e) MS-AuNR (I_{high} = 2 mM NaCl), and the impact of zeta potential, (c) -23 mV (MS-AuNR) and (g) -12 mV (PEG-MS-AuNR). Similar behavior is seen for longer AuNR with a larger aspect ratio of 6.8 (i and j). Quantitative details are summarized in Table 1.

This absorption is driven by the lower surface tension of a PEG−PS interface than the initial, relatively high interfacial energy between PS and water (25.8 mJ/m^2).[33] In contrast, PEG-AuNR do not remain absorbed on the P2VP surface after washing (Figure 2a). The relative change in hydrophobic interaction between the

**TABLE 1. Packing of Functionalized AuNR on Unpatterned Surfaces**

functionalized AuNR	surface	Figure	av no. AuNR/ 1000 nm^2	av center to center spacing, AuNR (nm)
PEG-AuNR[a]	PS	2b	195	95 ± 20
MS-AuNR(I_{low})[a,c]	P2VP	2c	287	85 ± 12
MS-AuNR(I_{high})[a,c]	P2VP	2e	650	50 ± 10
PEG-MS-AuNR[a]	P2VP	2g	475	62 ± 12
MS-AuNR(I_{low})[b,c]	P2VP	2i	230	70 ± 10

[a] AuNR (length = 47.8 ± 5 nm, diameter = 20.0 ± 3 nm). [b] AuNR (length = 76.5 nm ±15 nm, diameter = 15.8 ± 2 nm). [c] I_{high} = high ionic strength (2 mM NaCl); I_{low} = low ionic strength (0.2 mM NaCl).

particle and P2VP is less than that between the particle and PS due to hydrogen bonding between the pyridine group and water.[34] This hydrogen bonding with water results in a slightly lower interfacial tension (17.8 mJ/m^2) and an additional enthalpic penalty for displacement of surface water by PEG. Also, note that the absence of absorption on P2VP indirectly confirms the effective coating of the AuNR with PEG since the relatively strong pyridine–Au interaction commonly used in ligand exchange reactions is inhibited.

In contrast to hydrophobic-based selective adsorption of PEG-AuNR to PS, electrostatics may be utilized to drive preferential absorption of electrostatically stabilized MS-AuNR to P2VP-functionalized regions (Figure 2c–j). The weakly basic P2VP (pyridine pK_a = 5.2) will be partially ionized (~20%) in the slightly acidic MS-AuNR solution (pH 5.5).[35] As a result, an ionic exchange creates an electrostatic couple between the negatively charged sulfonate and positively charged protonated pyridine.[36] The resulting change in surface charge as the density of MS-AuNR on the surface increases self-limits further absorption of multilayers of MS-AuNR. Additionally, the spatial extent of the particle–particle repulsion will determine the maximum surface coverage of AuNR. At high electrolyte content, the additional salt screens surface charge and reduces the electrical double layer (Debye length). For example, a MS-AuNR solution with 2 mM NaCl results in over twice the particle density than a MS-AuNR solution with 0.2 mM NaCl. The electrostatically driven absorption also provides preferential absorption of AuNR of different aspect ratio (6.8) and different zeta potential (−12.0 mV). Also, note that control experiments confirm the absence of MS-AuNR absorption on bare silica (*i.e.*, substrate underlying the PDSP pattern). At pH's greater than silica's pK_a (~2–3), the surface silanol groups are partially ionized to Si–O$^-$, creating an effective negative surface charge and repelling negatively charged MS-AuNR.

The greater tunablility of long-range electrostatic interactions relative to steric stabilization provides a facile approach to assess the impact of confinement on absorption and local particle order through change of solution ionic strength and pH. Figure 3 summarizes
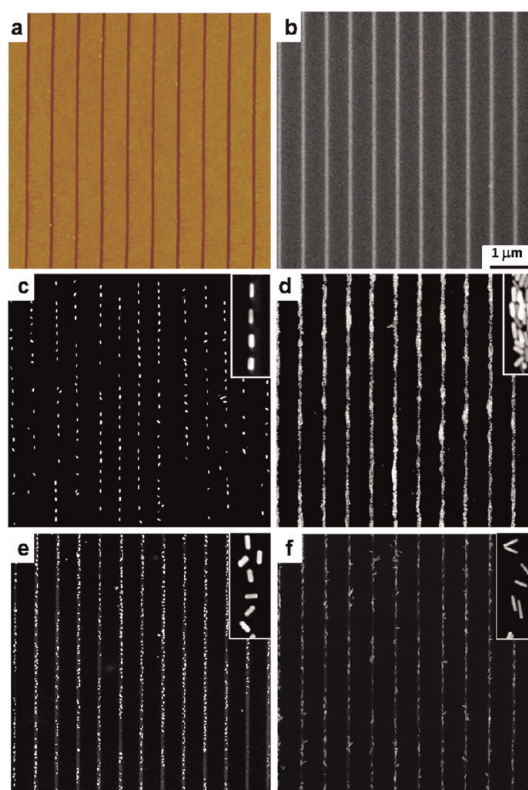
Figure 3. Tunability and selectivity of AuNR assembly on P2VP–PS chemical contrast surface patterns. AFM (a) and SEM (b) images of the initial chemical contrast pattern (SEM: light-P2VP and dark-PS). After assembly (AuNR length = 47.8 ± 5 nm, diameter = 20.0 ± 3 nm), SEM confirms selectivity of the MS-AuNR onto the P2VP domain and shows the impact of electrolyte content, (c) MS-AuNR (I_{low} = 0.2 mM NaCl) and (d) MS-AuNR (I_{high} = 2 mM NaCl), and the impact of zeta potential, (c) −23 mV (MS-AuNR) and (e) −12 mV (PEG-MS-AuNR). Similar behavior is seen for longer AuNR with a larger aspect ratio of 6.8 (f). The scale bar represents 1 μm. The inset in each part (c–f) shows a high-magnification image of the local arrangement of the AuNR.

the impact of electrostatic conditions on the selectivity of MS-AuNR to P2VP stripes (50 nm wide: Figure 3a, 3b, 3d, 3e and 3f; 30 nm wide: Figure 3c) in a background of PS. AFM and SEM confirm a uniform surface pattern with minimal topographic contrast (<3 nm) between the light PS background and darker P2VP lines (AFM).[28] Note that contrast observed in the SEM results from the difference in secondary electron yield and charge transport between the PS and P2VP.[37] At intermediate to high electrolyte content (0.7–2 mM), dense assemblies of AuNR occur on the P2VP stripes. In contrast to the random orientation of AuNR within the large areas, the confining line forces uniform orientation of the AuNR parallel to the PS–P2VP boundary. However, the AuNR assembly is broader and more irregular than the underlying P2VP feature. Reducing the electrolyte concentration (0.2 mM) and thus increasing particle–particle repulsion provide even cleaner replication of the underlying chemical pattern. AuNR density is lower, and the uniformity of particle–particle spacing and
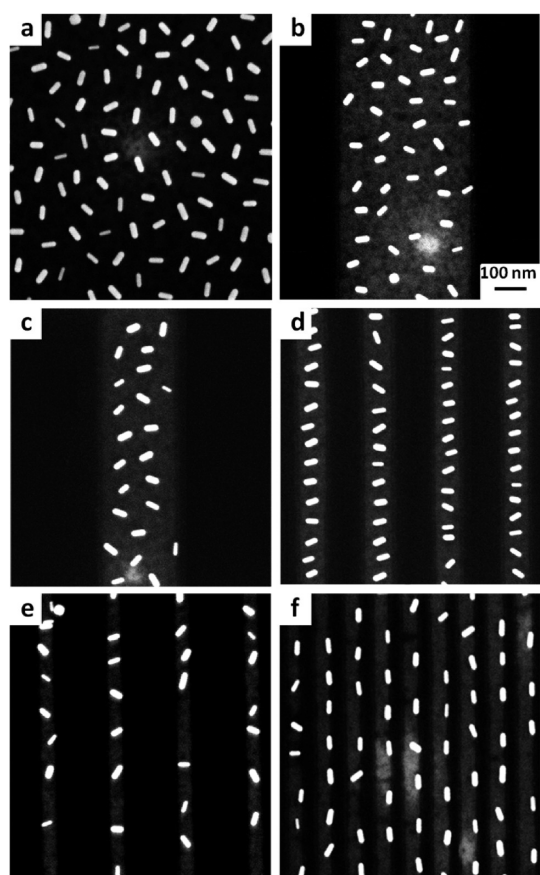
Figure 4. Particle ordering within directed assemblies of MS-AuNR on P2VP−PS contrast pattern created with conditions favoring long-range particle−particle repulsion. At low electrolyte content (0.2 mM NaCl), AuNR orientation is controlled by the width of the P2VP pattern, (a) blank P2VP pattern (no confinement), and decreasing nominal width of the pattern, (b) 500 nm, (c) 250 nm, (d) 100 nm, (e) 50 nm, and (f) 30 nm. The scale bar for SEM images represents 100 nm. Quantitative details are summarized in Table 2.

TABLE 2. Orientation and Spacing of AuNR on P2VP−PS Chemical Contrast Patterns[a]

P2VP pattern width (nm)	Figure	AuNR angle (deg)[b]	av center to center spacing, AuNR (nm)
497.5 ± 7.5	4b	84.4 ± 25.7	98.5 ± 10.2
254.1 ± 5.1	4c	85.7 ± 17.9	95.3 ± 11.5
116.5 ± 3.3	4d	87.5 ± 28.1	84.4 ± 8.7
49.1 ± 1.8	4e	46.7 ± 15.1	90.5 ± 20.1
30 ± 1.5	4f	11.5 ± 7.1	98.5 ± 14.2

[a] MS-AuNR (I_{low}): 0.2 mM NaCl; AuNR length = 47.8 ± 5.0 nm, AuNR diameter = 20.0 ± 3.0 nm. [b] Orientation angle = 0 for long axis of AuNR parallel to pattern boundary.

relative orientation is substantially greater. Similar pattern replication is also possible with longer AuNR and lower zeta potentials.

To demonstrate the impact of the chemical pattern geometry on assembly, Figure 4 illustrates the dependence of local nanorod spacing and orientation for absorption of MS-AuNR (0.2 mM) on P2VP stripes with widths from 500 to 30 nm. At 500 nm stripe width (Figure 4b), the AuNR adopt a local arrangement that minimizes orientational disorder between AuNR. Furthermore this local order extends across the pattern width and results in a mesoscopic order where the long axis of the AuNR is perpendicular to pattern axis. Such hierarchical arrangement is completely absent on a large area of P2VP surface (Figure 4a) and increases in occurrence when the pattern width is 6−10 times the AuNR size. This ordered AuNR arrangement maximizes packing within the chemical pattern by minimizing fractional area at the P2VP−PS boundary. The mean spacing between the centers of the rods is similar in both cases, 98.5 ± 10.2 at 500 nm pattern width and

85 ± 12 nm on the unpatterned P2VP surface. This confirms that similar particle−particle interactions are dictating the in-plane particle spacing in both instances. Furthermore, the presence of a long-range spatial and orientational order implies the process of assembly is not random sequential absorption, but that an approaching AuNR responds with changes in both orientation and translation of the chemical pattern. At this juncture though, additional studies systematically altering particle−surface binding are necessary to determine if upon approach the AuNR adjusts to the chemical pattern and previously absorbed particles or the previously absorbed particles adjust in plane to the approaching AuNR to maximize area fraction. Nevertheless, the width of the pattern directly controls the position and orientation of the AuNR. At 250 nm pattern width (Figure 4c) AuNR are assembled parallel to each other in two columns with similar spacing. As the confinement decreases to 100 nm (Figure 4d), the available space for the AuNR decreases such that only one column oriented perpendicular to the strip forms. Further narrowing of the feature width shifts the orientation of the rods relative to the P2VP−PS boundary. At 50 nm width (Figure 4e), the AuNR adopt a tilted orientation, whereas at 30 nm the AuNR assemble end-to-end and parallel to the feature axis. In all cases the average particle spacing is similar (Table 2). Note that as the line width decreases, irregularities in absorption density occur along the line length. We believe these reflect local irregularities in the underlying chemical P2VP−PS pattern due to side effects of the processing steps such as photoresist residue, base developer, or photon damage.[28] The overall behavior of AuNR absorption, that is, constant particle spacing and a pattern width dependent local orientation, implies that the mechanism of absorption for these solution conditions allows for maximization of particle packing and thus the minimization of free energy due to the creation of favorable particle−surface interactions. Thus particle packing should be related to the maximum covered area fraction given the geometric features of the AuNR and the pattern. As a simple geometric model, consider that the effective size of the AuNR

can be expressed as the particle area plus the area excluded due to electrostatic repulsion. This excluded distance is approximated by the Debye screening length, κ^{-1}. Thus the absorbed area per particle is $(\ell + 2\kappa^{-1})(d + 2\kappa^{-1})$, where ℓ and d are the length and diameter of the AuNR. The width of the pattern is λ (Figure 1). Normalized distance is defined relative to the smallest geometric feature of the AuNR, d, such that $L^* = \ell/d$, $\kappa^{-1*} = \kappa^{-1}/d$, and $\lambda^* = \lambda/d$. The preferred NR structure will then be the one that arranges the AuNR to maximize the fractional area covered within the feature width (see Supporting Information, S.IV. for details of the model and calculation).

Based on these simple geometric packing considerations, Figure 5 summarizes the effective phase diagram assuming the two most basic possible packing geometries (orientation parallel or perpendicular to the feature axis) for AuNR of aspect ratio 2.5 as a function of feature width and Debye screening length. For the MS-AuNR in Figure 4, $\ell = 50$ nm, $d = 20$ nm, and $\kappa^{-1} \approx 19.5$ nm. The latter is the approximated solution measurement of the diffuse electric double layer assuming spherical particles (see Supporting Information, S.II.).[33] Note that this estimate is consistent with the 35 nm mean spacing between AuNR surfaces observed on the large-area P2VP regions, which should be close to $2\kappa^{-1}$ if the final absorbed structure is dominated by electrostatics. In general, for $\lambda^* < 1$ particles cannot absorb. For $\lambda^* < L^*$, the only possible arrangement is for the rods to form columns with their long axis parallel or tilted to the feature axis. For $\lambda^* > L^*$, arrangements where the long axis of the rod is perpendicular to the feature axis become possible. For a given feature width, the maximum packing depends on the area excluded due to electrostatic interactions and thus on κ^{-1*}. As κ^{-1*} increases, the effective size of the AuNR will increase, and the transition between different packing arrangements will occur at larger pattern widths, λ^*. The black filled circles in Figure 5 denote the experimental conditions discussed in Figure 4. The particle packing observed for these conditions agrees very well with predicted phase behavior. The exception is for the largest spacing, $\lambda = 250$ nm, which exhibits a structure that is predicted to occur at a slightly lower stripe width. The general agreement reinforces the supposition that local particle spacing and orientation is driven by a balance between particle–surface attraction and particle–particle repulsion. Overall, local maximum packing geometries that are more complex than parallel or perpendicular to the feature axis can be envisioned. In addition to the effective tilting seen in Figure 4e, more complex local-particle packing arrangements were also observed at other conditions (particle surface chemistry and pattern size and spacing). These included chiral-like arrangements where the relative angle between successive AuNR and the pattern edge
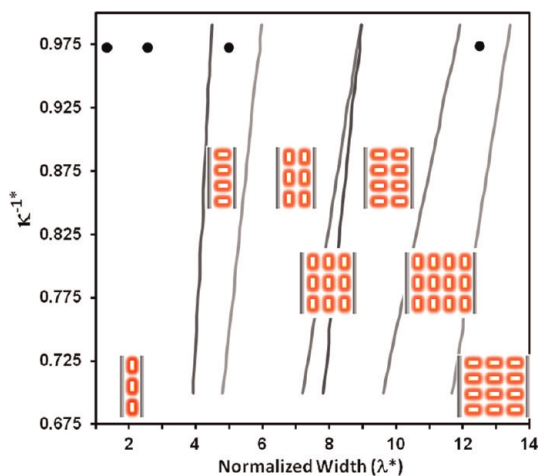
Figure 5. Preferred packing structure based on maximization of surface coverage with regard to normalized Debye length (κ^{-1*}) and pattern width (λ^*) for AuNR with an aspect ratio of 2.5. κ^{-1*} and λ^* are normalized with respect to AuNR diameter. The lines denote the boundary between various structures with orientation parallel and perpendicular to the stripe boundary (as shown in the schematics). Black filled circles correspond to the experimental conditions used for Figure 4, from left (Figure 4f), (Figure 4e), (Figure 4d), and (Figure 4c) showing reasonable agreement between predicted and observed AuNR arrangements.

evolved from 0° to 90° in analogy with previous discussions on symmetry breaking of block copolymers in pores[25] (Supporting Information, Figure S9). Also, when feature spacing was small, lateral registry of AuNR on adjacent features occurred (Supporting Information, Figure S10). This implies that long-range electrostatic interactions between particles can drive particle arrangements both within *and* between chemical patterns. A detailed understanding of these complex structures necessitates a more refined model that explicitly considers the nonspherical particle–particle interactions and shape.

CONCLUSIONS

The use of lithographically defined, chemically nanopatterned surfaces and tailored particle–particle surface interactions for fabricating arrays and cluster arrays of nanoparticles is of importance from fundamental and technological perspectives. The starting point for assembly is precise patterns with densities and resolution of features that are conveniently and inexpensively created over large areas using standard tools of the semiconductor industry. The lithographic templates alone, however, are often not of high enough resolution to be the same characteristic dimension of the nanoparticles, nor do the templates have inherent function. Using the massively parallel process of site-specific adsorption of nanoparticles from solution onto surfaces, particle–surface interactions can be engineered to control the locations of particles, and particle–particle interactions in combination with confining pattern geometry can be engineered to control

particle spacing and orientation with respect to the pattern and other particles. Particle size, in a sense, defines the resolution of the hierarchically ordered system. In this work, we have chosen commensurate surface and particle chemistries to induce attractive and repulsive electrostatic forces as a driving force for hierarchical assembly so as to take advantage of the versatile nature of these interactions at long and short range. The interaction between MS-AuNR and P2VP-functionalized regions is attractive, particle—particle interactions are repulsive, and the balance of forces results in uniform interorder spacing and confinement-dependent orientation. A number of additional factors influence the assembly yield, and their further optimization is likely to afford strong improvements in the assembly process with suppression of defect formation. Additional functionalities can be conferred to such building blocks through conjugation with molecular functionality that exhibit particular biological, electrical, and optical properties. Challenges still remain though for making more complex architectures such as chiral or more hierarchical structures. Nevertheless, large-scale organization of arrays of and cluster arrays of nanoparticles provide opportunities for many advanced applications, including those derived from the anisotropic optical properties arising from hybridized plasmon modes associated with the engineered coupling of the AuNR plasmon resonances.

METHODS

Materials. Hexadecyltrimethylammonium bromide (98%), benzyldimethylammonium chloride hydrate (BDAC) (98%), and L-ascorbic acid were purchased from Tokyo Chemical Industry. Chloroauric acid ($HAuCl_4$) (99.999%), sodium borohydride ($NaBH_4$) (>95%), and mercaptopropane sulfonate sodium salt (MS) were purchased from Sigma-Aldrich. Silver nitrate ($AgNO_3$) (electrophoresis grade) was purchased from ACROS, and thiolated poly(ethylene glycol) (PEG-SH) was purchased from Nanocs Inc. All chemicals were used as received without further purification. Deionized water (18.2 MΩ), obtained from Branstead Nanopure System, was used in all the experiments.

Characterization. UV—vis—NIR spectra were acquired with a Cary 5000 UV—visible—near IR spectrophotometer. Zeta potential data were acquired with Zetasizer Nano from Malvern. The sizes of AuNR were examined by TEM (Philips CM200 LaB6 at 200 kV), and the morphology on the surfaces was analyzed using HR-SEM (Sirion, FEI Company, USA).

Gold Nanorod Synthesis. AuNR were synthesized by the seed-mediated growth process in CTAB solutions in the presence of $AgNO_3$, as reported previously.[5,38] To ensure reproducibility of the subsequent steps, we set the temperature at 25 °C for all reactions. The growth solution was prepared by mixing $HAuCl_4$ (0.5 mL, 0.1 M), $AgNO_3$ (0.08 mL, 0.1 M), and CTAB (100 mL, 0.1 M) followed by adding into the solution ascorbic acid (0.55 mL, 0.1 M) as a mild reducing agent. The seed solution was prepared by dissolving $HAuCl_4$ (0.025 mL, 0.1 M) in an aqueous solution of CTAB (10 mL, 0.1 M). The bright yellow transparent solution was stirred for 1 h. A freshly prepared, ice-cold $NaBH_4$ solution (0.6 mL, 0.01 M) was then added into the mixture under vigorous stirring. After 5 min, 0.1 mL of this seed solution was added into the previously prepared growth solution and shaken for 5 min. The color of the reaction solution slowly changed from clear to violet and finally green (for aspect ratio 2.5), indicating the growth of AuNR. To synthesize AuNR of aspect ratio 6.8, the growth solution was prepared with a mixture of surfactant and CTAB/BDAC (CTAB 0.1 M, BDAC 0.125 M in 100 mL). The as-made AuNR solution (or the solution of interest) was kept in an Erlenmeyer flask at 25 °C for 15 h. The solution was then centrifuged at 7500 rpm for 1 h, and the brownish-green residue (from bottom) (in ~10% of supernatant) was carefully collected, leaving behind a pink residue on the tube sidewalls. The purified AuNR product (collected residue) was stored at 25 °C in a closed glass vial. Concentrations of NR were calculated using $\varepsilon = 1.425 \times 10^9$ or 6.041×10^9 M^{-1} cm^{-1} for aspect ratio of 2.5 and 6.8, respectively, as reported for previous methods.[5,38]

AuNR Functionalization: Place Exchange Reaction. In order to develop selectivity of AuNR on polymer surfaces of polystyrene and poly(2-vinylpyridine), place exchange reaction on AuNR surface was carried out. This was done by replacing CTAB with PEG-SH and MS, making them selective on the PS and P2VP surface, respectively. Figure S1 shows the schematic diagram of the place exchange reaction process. At first, CTAB was replaced by PEG-SH, which changes the initial positively charged AuNR (+40 mV) into neutral charged (−2 mV). The next step of ligand exchange was done by adding MS to make the AuNR negatively charged (−23 mV). Throughout the process, the AuNR must remain individually isolated within the aqueous solution. The zeta potential and UV—vis spectra (Figure S2) were monitored at each step of the reaction to analyze overall surface charge and assess the stability of AuNR in the aqueous solution.

PEGylation of AuNR (PEG-AuNR). A 1 mM aqueous solution of PEG-SH (20K) was prepared from freshly sonicated water (5 min). The latter step removes dissolved oxygen, which helps to ensure active thiol groups in PEG instead of dithiol formation. A freshly prepared AuNR solution was centrifuged at 10 000 rpm for 10 min to remove excess CTAB. Supernatant was discarded, and the PEG aqueous solution was added into the residue to make a 2 nM AuNR solution. The mixture was vortexed for 2 min and kept at room temperature for 48 h. At this stage the zeta potential of the product was +15 mV (original CTAB AuNR is +40 mV), confirming partial functionalization of the AuNR surface by PEG-SH. This is possibly the result of selective end functionalization of AuNR by PEG-SH due to the much stronger binding of the CTAB bilayer to the AuNR side. The rod ends consist of {301} and {310} planes[39] and are believed to frustrate CTAB absorption and packing, whereas the side facets of the rod {0512} are believed to support a robust CTAB bilayer.[39,40] To replace CTAB by PEG-SH on all the surfaces of the AuNR, the initial solution product was centrifuged at 10 000 rpm for 15 min. The supernatant was discarded, and the next step of functionalization was done by dissolving the residue with 5 mM PEG-SH (5K) and storing at room temperature for 48 h. Here, dissolving the AuNR residue by PEG-SH aqueous solution disturbs the CTAB bilayer by further reducing the overall CTAB solution concentration below the critical micelle concentration. After the reaction and centrifugation step (10 000 rpm for 15 min), the residue was again dissolved into 5 mM PEG-SH (5K). UV—vis spectra of this solution (PEG-AuNR) showed a plasmon band similar to the pristine NR, confirming individual dispersion of AuNR (Figure S2). At this stage, the zeta potential of the product was −2 mV, confirming successful ligand exchange of all the CTAB by PEG-SH. Here the PEG chain provides steric stabilization to the AuNR, which keeps them individually isolated in the aqueous solution. It is important to note that, for AuNR of aspect ratio 2.5, PEG-SH (20K) was used for end functionalization, and PEG-SH (5K) was used for side functionalization. We found that at the ends, PEG-SH (20K) gave AuNR more stability in the aqueous solution than with PEG-5K and thus enables the additional exchange steps. However, using PEG-SH (20K) or PEG-SH (5K) at the sides did not have any noticeable effect

on subsequent stabilization of AuNR. Thus for the smaller AuNR, PEG-SH (5K) was preferred because of its faster reactivity than that of PEG-SH (20K). However, for the larger AuNR (aspect ratio 6.8), PEG-SH (20K) on the sides was necessary to ensure stability.

Sulfonation of AuNR (MS-AuNR). A 20 mM MS solution was prepared in freshly sonicated water (5 min). A 5 mL amount of MS aqueous solution was added into 5 mL of PEG-AuNR solution. The mixture was vortexed for 5 min and kept at 40 °C for 7 h. The mixture was then kept at room temperature for a week. At this stage, the zeta potential of the product was −12 mV, confirming partial ligand exchange of PEG-SH by MS. To have complete place exchange with MS, the product was centrifuged at 10 000 rpm for 15 min. The supernatant was discarded, and the next step of functionalization was done by dissolving the residue with 2 mM MS. The reaction solution was vortexed for 5 min and kept at 40 °C for 7 h, followed by keeping at room temperature for another 1 week. At this stage, the zeta potential of the product was −23 mV, confirming successful ligand exchange of PEG-SH by MS. Here the negatively charged sulfonate group gives electrostatic stabilization to AuNR, which makes it possible to individually disperse them into the aqueous solution (Figure S2).

Directed Assembly of AuNR on Polymer Surfaces. The polymer-derived surface pattern and the plain polymer surfaces were prepared as reported elsewhere.[28,41,42] For the assembly, a substrate was dipped into aqueous solutions of a functionalized AuNR and kept at room temperature. After 30 min, it was first rinsed with water then dipped into a glass vial containing DI water and sonicated (bath) for 15 min. Finally it was taken out from the vial, rinsed again with DI water, and dried by N₂.

Conflict of Interest: The authors declare no competing financial interest.

Supporting Information Available: Schematics of place exchange reaction on AuNR surface (Figure S1), UV−vis spectra of AuNR in solution (Figure S2), details and discussion on the calculation of interfacial free energy (S.I.), estimation of AuNR Debye length (S.II.), fast Fourier transform of AuNR assembly on the pattern surfaces (S.III.), modeling of the AuNR orientation in response to a confined surface pattern (S.IV.), and SEM images of additional complex local particle packing arrangements (S.V.). This material is available free of charge via the Internet at http://pubs.acs.org.

REFERENCES AND NOTES

1. Halas, N. J.; Lal, S.; Chang, W.-S.; Link, S.; Nordlander, P. Plasmons in Strongly Coupled Metallic Nanostructures. *Chem. Rev.* **2011**, *111*, 3913–3961.
2. Gramotnev, D. K.; Bozhevolnyi, S. I. Plasmonics beyond the Diffraction Limit. *Nat. Photonics* **2010**, *4*, 83–91.
3. Ghosh, S. K.; Pal, T. Interparticle Coupling Effect on the Surface Plasmon Resonance of Gold Nanoparticles: From Theory to Applications. *Chem. Rev.* **2007**, *107*, 4797–4862.
4. Zhao, J.; Frank, B.; Burger, S.; Giessen, H. Large-Area High-Quality Plasmonic Oligomers Fabricated by Angle-Controlled Colloidal Nanolithography. *ACS Nano* **2011**, *5*, 9009–9016.
5. Nepal, D.; Park, K.; Vaia, R. A. High-Yield Assembly of Soluble and Stable Gold Nanorod Pairs for High-Temperature Plasmonics. *Small* **2012**, *8*, 1013–1020.
6. Mann, S. Self-Assembly and Transformation of Hybrid Nano-Objects and Nanostructures under Equilibrium and Non-Equilibrium Conditions. *Nat. Mater.* **2009**, *8*, 781–792.
7. Li, F.; Josephson, D. P.; Stein, A. Colloidal Assembly: The Road from Particles to Colloidal Molecules and Crystals. *Angew. Chem., Int. Ed.* **2011**, *50*, 360–388.
8. Wang, Y.; Chen, G.; Yang, M.; Silber, G.; Xing, S.; Tan, L. H.; Wang, F.; Feng, Y.; Liu, X.; Li, S.; Chen, H. A Systems Approach Towards the Stoichiometry-Controlled Hetero-Assembly of Nanoparticles. *Nat. Commun.* **2010**, *1*, 87.
9. Nie, Z.; Fava, D.; Kumacheva, E.; Zou, S.; Walker, G. C.; Rubinstein, M. Self-Assembly of Metal-Polymer Analogues of Amphiphilic Triblock Copolymers. *Nat. Mater.* **2007**, *6*, 609–614.
10. Thorkelsson, K.; Mastroianni, A. J.; Ercius, P.; Xu, T. Direct Nanorod Assembly Using Block Copolymer-Based Supramolecules. *Nano Lett.* **2012**, *12*, 498–504.
11. Romo-Herrera, J. M.; Alvarez-Puebla, R. A.; Liz-Marzan, L. M. Controlled Assembly of Plasmonic Colloidal Nanoparticle Clusters. *Nanoscale* **2011**, *3*, 1304–1315.
12. Hore, M. J. A.; Composto, R. J. Nanorod Self-Assembly for Tuning Optical Absorption. *ACS Nano* **2011**, *4*, 6941–6949.
13. Koh, S. Strategies for Controlled Placement of Nanoscale Building Blocks. *Nano Res. Lett.* **2007**, *2*, 519–545.
14. Pavan, M. J.; Shenhar, R. Two-Dimensional Nanoparticle Organization Using Block Copolymer Thin Films as Templates. *J. Mat. Chem.* **2011**, *21*, 2028–2040.
15. Yin, Y.; Lu, Y.; Gates, B.; Xia, Y. Template-Assisted Self-Assembly: A Practical Route to Complex Aggregates of Monodispersed Colloids with Well-Defined Sizes, Shapes, and Structures. *J. Am. Chem. Soc.* **2001**, *123*, 8718–8729.
16. Son, J. G.; Bae, W. K.; Kang, H.; Nealey, P. F.; Char, K. Placement Control of Nanomaterial Arrays on the Surface-Reconstructed Block Copolymer Thin Films. *ACS Nano* **2009**, *3*, 3927–3934.
17. Jang, S. G.; Kramer, E. J.; Hawker, C. J. Controlled Supramolecular Assembly of Micelle-Like Gold Nanoparticles in PS-B-P2VP Diblock Copolymers via Hydrogen Bonding. *J. Am. Chem. Soc.* **2011**, *133*, 16986–16996.
18. Lin, Y.; Daga, V. K.; Anderson, E. R.; Gido, S. P.; Watkins, J. J. Nanoparticle-Driven Assembly of Block Copolymers: A Simple Route to Ordered Hybrid Materials. *J. Am. Chem. Soc.* **2011**, *133*, 6513–6516.
19. Hung, A. M.; Micheel, C. M.; Bozano, L. D.; Osterbur, L. W.; Wallraff, G. M.; Cha, J. N. Large-Area Spatially Ordered Arrays of Gold Nanoparticles Directed by Lithographically Confined DNA Origami. *Nat. Nanotechnol.* **2010**, *5*, 121–126.
20. Ma, L.-C.; Subramanian, R.; Huang, H.-W.; Ray, V.; Kim, C.-U.; Koh, S. J. Electrostatic Funneling for Precise Nanoparticle Placement: A Route to Wafer-Scale Integration. *Nano Lett.* **2007**, *7*, 439–445.
21. Jiang, L.; Wang, W.; Fuchs, H.; Chi, L. One-Dimensional Arrangement of Gold Nanoparticles with Tunable Interparticle Distance. *Small* **2009**, *5*, 2819–2822.
22. Jiang, L.; Sun, Y.; Nowak, C.; Kibrom, A.; Zou, C.; Ma, J.; Fuchs, H.; Li, S.; Chi, L.; Chen, X. Patterning of Plasmonic Nanoparticles into Multiplexed One-Dimensional Arrays Based on Spatially Modulated Electrostatic Potential. *ACS Nano* **2011**, *5*, 8288–8294.
23. Zou, S.; Hong, R.; Emrick, T.; Walker, G. C. Ordered Cdse Nanoparticles within Self-Assembled Block Copolymer Domains on Surfaces. *Langmuir* **2007**, *23*, 1612–1614.
24. Winkler, K.; Paszewski, M.; Kalwarczyk, T.; Kalwarczyk, E.; Wojciechowski, T.; Gorecka, E.; Pociecha, D.; Holyst, R.; Fialkowski, M. Ionic Strength-Controlled Deposition of Charged Nanoparticles on a Solid Substrate. *J. Phys. Chem. C* **2011**, *115*, 19096–19103.
25. Pickett, G. T.; Gross, M.; Okuyama, H. Spontaneous Chirality in Simple Systems. *Phys. Rev. Lett.* **2000**, *85*, 3652–3655.
26. Kuemin, C.; Stutz, R.; Spencer, N. D.; Wolf, H. Precise Placement of Gold Nanorods by Capillary Assembly. *Langmuir* **2011**, *27*, 6305–6310.
27. Holzner, F.; Kuemin, C.; Paul, P.; Hedrick, J. L.; Wolf, H.; Spencer, N. D.; Duerig, U.; Knoll, A. W. Directed Placement of Gold Nanorods Using a Removable Template for Guided Assembly. *Nano Lett.* **2011**, *11*, 3957–3962.
28. Liu, C.-C.; Han, E.; Onses, M. S.; Thode, C. J.; Ji, S.; Gopalan, P.; Nealey, P. F. Fabrication of Lithographically Defined Chemically Patterned Polymer Brushes and Mats. *Macromolecules* **2011**, *44*, 1876–1885.
29. Gentili, D.; Ori, G.; Franchini, M. C. Double Phase Transfer of Gold Nanorods for Surface Functionalization and

Entrapment into Peg-Based Nanocarriers. *Chem. Commun.* **2009**, 5874–5876.

30. Aizenberg, J.; Braun, P. V.; Wiltzius, P. Patterned Colloidal Deposition Controlled by Electrostatic and Capillary Forces. *Phys. Rev. Lett.* **2000**, *84*, 2997–3000.

31. Evans, J. W. Random and Cooperative Sequential Adsorption. *Rev. Mod. Phys.* **1993**, *65*, 1281.

32. Gray, J. J.; Bonnecaze, R. T. Adsorption of Colloidal Particles by Brownian Dynamics Simulation: Kinetics and Surface Structures. *J. Chem. Phys.* **2001**, *114*, 1366–1381.

33. Israelachvili, J. N. *Intermolecular and Surface Forces*; Academic Press: New York, 2010.

34. Schlücker, S.; Singh, R. K.; Asthana, B. P.; Popp, J.; Kiefer, W. Hydrogen-Bonded Pyridine−Water Complexes Studied by Density Functional Theory and Raman Spectroscopy. *J. Phys. Chem. A* **2001**, *105*, 9983–9989.

35. Chung, B.; Choi, M.; Ree, M.; Jung, J. C.; Zin, W. C.; Chang, T. Subphase pH Effect on Surface Micelle of Polystyrene-B-Poly(2-Vinylpyridine) Diblock Copolymers at the Air−Water Interface. *Macromolecules* **2005**, *39*, 684–689.

36. Perahia, D.; Pullman, A.; Pullman, B. Cation-Binding to Biomolecules. *Theor. Chim. Acta* **1977**, *43*, 207–214.

37. Sawyer, L. C.; Grubb, D. T. *Polymer Microscopy*, 2nd ed.; Chapman & Hall: London, 1996.

38. Park, K.; Koerner, H.; Vaia, R. A. Depletion-Induced Shape and Size Selection of Gold Nanoparticles. *Nano Lett.* **2010**, *10*, 1433–1439.

39. Katz-Boon, H.; Rossouw, C. J.; Weyland, M.; Funston, A. M.; Mulvaney, P.; Etheridge, J. Three-Dimensional Morphology and Crystallography of Gold Nanorods. *Nano Lett.* **2011**, *11*, 273–278.

40. Carbó-Argibay, E.; Rodríguez-González, B.; Gómez-Graña, S.; Guerrero-Martínez, A.; Pastoriza-Santos, I.; Pérez-Juste, J.; Liz-Marzán, L. M. The Crystalline Structure of Gold Nanorods Revisited: Evidence for Higher-Index Lateral Facets. *Angew. Chem., Int. Ed.* **2010**, *49*, 9397–9400.

41. Onses, M. S.; Liu, C. C.; Thode, C. J.; Nealey, P. F. Highly Selective Immobilization of Au Nanoparticles onto Isolated and Dense Nanopatterns of Poly(2-vinyl pyridine) Brushes down to Single-Particle Resolution. *Langmuir* **2012**, *28*, 7299–7307.

42. Onses, M. S.; Thode, C. J.; Liu, C. C.; Ji, S. X.; Cook, P. L.; Himpsel, F. J.; Nealey, P. F. Site-Specific Placement of Au Nanoparticles on Chemical Nanopatterns Prepared by Molecular Transfer Printing Using Block-Copolymer Films. *Adv. Funct. Mater.* **2011**, *21*, 3074–3082.